Room-Temperature Epitaxy of Metal Thin Films on Tungsten Diselenide

Kayla A. Cooley[1], Rajeh Alsaadi[1], Ramya L. Gurunathan[1], Anna C. Domask[1], Lauren Kerstetter[1], Wissam A. Saidi[2], and Suzanne E. Mohney[1]

[1] *Department of Materials Science and Engineering, The Pennsylvania State University, University Park, PA 16808, United States*
[2] *Department of Mechanical Engineering and Materials Science, University of Pittsburgh, Pittsburgh, PA 15261, United States*

ABSTRACT

The orientation of selected metals (Pd, Ni, Al, and Co) deposited on WSe_2 by physical vapor deposition was examined using transmission electron microscopy and selected area electron diffraction. We discovered that Ni demonstrates room-temperature epitaxy, similarly to other face centered cubic (FCC) metals Au, Ag, and Cu. These epitaxial metals exhibit the following orientation relationship, where M stands for metal: $M(111) \parallel WSe_2 (0001)$; $M[2\bar{2}0] \parallel WSe_2 [11\bar{2}0]$. Hexagonally close-packed Co, and FCC Pd and Al, were not epitaxial on deposition; however, Pd became epitaxial after annealing at 673 K for 5 h. To uncover critical variables for epitaxial growth, we correlated our experimental work and reports from the literature on Cu, Ag, and Au with density functional theory calculations of the energetics of metal atoms on the surface of WSe_2 and thermodynamic calculations of metal-W-Se phase equilibria. Furthermore, we compared the findings to our previous work on metal/MoS_2 systems to draw conclusions more generally applicable to epitaxial growth of metals on transition metal dichalcogenides (TMDs). We observed that epitaxy of metals on TMDs can occur when there is a match in crystallographic symmetry, even with a large lattice mismatch, and it is favored by metals exhibiting a low diffusion barrier on the TMD surface. However, reaction processes between the metal and WSe_2 can prevent epitaxy even when the other factors are favorable, as occurred for Al/WSe_2 with the formation of

aluminum selenide, tungsten aluminide, and elemental tungsten. Consideration of crystallographic symmetry, surface diffusion barriers, and reactivity can be used to predict room-temperature epitaxy in other metal/TMD systems.

I.   INTRODUCTION

Of the many emerging 2D materials, transition metal dichalcogenides (TMDs), like MoS_2 and WSe_2, are attractive for electronic and photonic devices as many of them are semiconducting when only a few layers thick[1], and they can be transferred onto flexible substrates[2,3]. Tungsten diselenide is especially promising for electronics applications since this material exhibits ambipolar characteristics as well as smaller effective masses for both holes and electrons than other TMDs[4]. Successful application of TMDs in commercial technology requires a fundamental understanding of the interfaces between TMDs and other materials, such as metals that can serve as electrical contacts. Room-temperature epitaxy of metals is an interesting phenomenon that has been observed on a number of TMDs, including Cu, Ag, and Au on both WSe_2[5-8] and WS_2[7,9,10]; Cu, Ag, Au, Pd, and Pd on MoS_2[11-17]; and Au and Cu on $MoTe_2$[18]. Much remains to be learned about this phenomenon, and further studies could offer new insights into quasi-van der Waals epitaxy for the development of novel heterostructures and for electrical contacts that may be altered or improved through epitaxy. High contact resistance between metals and TMDs is a continuing problem for device development[19,20], and it has been shown that differences in the Schottky barrier height at a metal contact can be affected by the atomic arrangement at the metal/semiconductor interface[21-23].

In our previous work, Domask *et al.*[24] investigated room-temperature epitaxy of transition metals on MoS_2. We discovered a number of metals that were epitaxial on MoS_2 not yet reported in the literature, including Zn, which is the only identified HCP metal exhibiting room-temperature epitaxy on MoS_2[24]. By comparing our experimental results with Saidi's density functional theory (DFT) calculations of the energetics of metal atoms on the surface of MoS_2[25], we determined that epitaxial metal/MoS_2 systems had a couple of characteristics in common: the close-packed plane of the metal with 6-fold symmetry was in contact with the basal plane of MoS_2 and the barrier to metal atom surface diffusion was low[24]. This study led us to ask if the factors favoring epitaxy would be the same for the metal/WSe_2 systems. If so, then the approach could be used more generally to predict epitaxy of metals on TMDs.

Literature concerning metal/WSe_2 epitaxy has been limited to the noble (Group XI) metals Cu, Ag, and Au. Jaegermann *et al.*[5] reported Cu and Ag to be epitaxial when deposited on WSe_2 at 100 K and studied the Schottky barrier formed at the atomically abrupt van der Waals interface, while Klein *et al.*[6] completed a similar study of Au and Cu deposited on WSe_2 at room temperature and 85 K. The Au/WSe_2 epitaxial system was also studied by Rettenberger *et al.*[7] who used scanning tunneling microscopy to examine the island growth of Au on WSe_2 from 300-580 K. Interestingly, Rettenberger *et al.*[7] noted differences in the epitaxial growth of Au on WS_2 and WSe_2 and hypothesized that these could be attributed to differences in lattice mismatch and/or ionic character of the TMD surfaces. Nicolay *et al.*[8] refuted the importance of lattice mismatch on epitaxial growth of Au and Ag deposited on WSe_2 at room temperature, revealing that the morphology of epitaxial metals could be affected by deposition rate and surface diffusion. They reported that Au and Ag demonstrated Volmer-Weber growth on the WSe_2 (0001) surface. Their work showed less corrugation and smoother surface topography when the metal was deposited at

a high rate and the substrate was cooled to suppress surface diffusion[8]. These studies provide important clues concerning the growth of noble metals on WSe_2, but the behavior of many other metal/WSe_2 systems remains unknown, and factors controlling this behavior should be further evaluated.

In pursuit of a deeper understanding of epitaxial metal/TMD systems, this work investigates selected metals (Al, Ni, Pd, and Co) deposited on WSe_2 at room temperature to identify metals exhibiting epitaxy on WSe_2, to compare metal/WSe_2 epitaxial relationships to those of MoS_2, and to determine if factors controlling this interesting behavior are the same for both MoS_2 and WSe_2.

II.   METHODS

Samples were prepared by mechanically exfoliating WSe_2 flakes onto Quantifoil® holey carbon TEM grids using Nitto thermal release tape. Metal overlayers were sputtered to a thickness of 30 nm using UHV DC magnetron sputtering at a rate of 1 Å/s. Each deposition had a starting base pressure less than 10^{-7} torr, and 5 mtorr ultra-high purity (UHP) Ar was used as the sputtering gas. Deposited metals included Ni, Pd, Co, and Al. Some samples were annealed to explore the effect of thermal processing. Annealing took place in a tube furnace at 673 K for either 4 or 5 h. Samples were annealed in an UHP Ar environment (100 sccm), with the Ar gettered with Zr before reaching the sample.

Transmission electron microscopy (TEM) and selected area electron diffraction (SAED) were performed in plan view using a FEI Talos F200X. An accelerating voltage of 80kV was used to reduce electron beam induced-damage of WSe_2. TEM was critical to finding the exfoliated

3

flakes on the TEM grids, and SAED determined the crystal structure and orientation of both the WSe$_2$ flakes and metal overlayers. The orientation relationship for epitaxy of metals on TMDs has been reported in literature[5,6-14,16-18,24], and we also find this relationship by comparing our diffraction patterns to predicted diffraction patterns of specific epitaxial metal/WSe$_2$ systems using the *JEMS Electron Microscopy Software* (v. 4.5331U2017). To ensure repeatability and avoid any effects from flake-to-flake variability, the epitaxial relationship (or lack thereof) was determined by analyzing at least three flakes for each metal/WSe$_2$ system. In addition, energy dispersive spectroscopy (EDS) using the built-in Super XEDS system on the Talos F200X was completed on each flake to elementally confirm flake identity and monitor contamination. Cross-sectional sample TEM samples were prepared using a Scios 2 FESEM or a Helios NanoLab 660 FESEM, both coupled with a focused ion beam (FIB). This preparation included ion-beam gas-assisted chemical vapor deposition of at least 1 μm thick carbon layer to protect the sample during milling. The elemental maps were collected using a TEM accelerating voltage of 200 kV. Scanning electron microscopy of the surface was also carried out on a small number of flakes using a ZEIS Merlin FESEM at 5 kV to examine metal grain size before and after annealing.

First-principles DFT calculations are carried out within the Perdew-Burke-Ehrenzhof (PBE)[26] exchange-correlation functional and projector augmented wave (PAW) pseudopotentials[27,28] as implemented in the Vienna Ab initio Simulation Package (VASP). The WSe$_2$ monolayer is modeled using a (3×3) surface supercell with 12 Å of vacuum in the non-periodic direction to mitigate fictitious interaction between periodic images. The adsorption configurations of a metal atom on the high symmetry sites of WSe$_2$ are illustrated in Figure 1. The integration over the Brillouin zone is limited to the Γ point only, as we adopt a relatively large

supercell. Diffusion barriers are computed using the climbing image nudged elastic band method with 3-5 images[29]. Overall the computational framework is similar to previous studies[30,31].
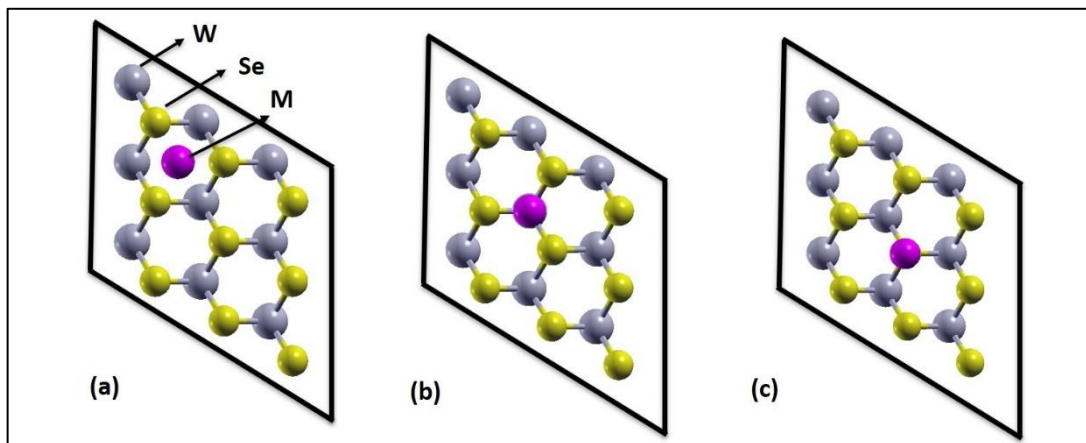

Figure 1. Adsorption configurations for a metal atom M at (a) hollow, (b) top W, and (c) top Se sites. WSe$_2$ is modeled using a (3 x 3) surface supercell. W, Se and the metal atom are shown as grey, gold and pink spheres, respectively.

For thermodynamic calculations of bulk phase equilibria, metal/WSe$_2$ systems were classified as WSe$_2$-dominant (for unreactive systems), metal selenide-dominant (for reactive systems), or indeterminant (for systems with insufficient thermodynamic data). Classification was determined from ternary phase diagrams calculated with the Schmid-Fetzer approach[32] using a MATLAB program we wrote. The primary source for binary phase diagrams and binary intermetallic compound lists was the *ASM Alloy Phase Diagram Database*[33]. The main sources of thermodynamic data for these intermetallic compounds were *Cohesion in Metals: Transition Metal Alloys* by de Boer[34], *Materials Thermochemistry* by Kubaschewski[35], and *The Chemical Thermodynamics of Selenium* by Olin[36]. In the compilation by Olin, when multiple entropy and

enthalpy values were provided for M-Se compounds, we selected the values that were chosen by the author [36]. Additionally, some of the enthalpy of formation values for the metal-W phases given in the de Boer text are approximations using the Miedema's estimate, as indicated in the data table[34]. Finally, if the entropy of formation was not provided for an intermetallic compound, the value was taken to be zero. Given that the reactions considered here are solid phase reactions, the entropy change is small in comparison to the enthalpy change, so this approximation is reasonable. The enthalpy of formation value for WSe_2 used in our study of -185.5 kJ/mol is obtained from a fluorine combustion calorimetry study by O'Hare, Lewis and Parkinson and was selected in the text by Olin[37]. The entropy of formation was approximated as zero. For the phase diagram calculation, all possible tie lines were generated, and in the case of an intersection of tie lines, the Gibb's free energy of reaction (ΔG_{rxn}^{o}) per atom was used to find the more stable pair of phases corresponding to the viable tie line. To account for the error bars in the thermodynamic data, a tie line was considered tentatively stable if the ΔG_{rxn}^{o} was less than 8,000 J/mol/atom in magnitude for every intersecting tie line that is found to be more stable. The sign of ΔG_{rxn}^{o} depends on whether the intersecting tie line is taken to be the products or reactants in the reaction. The calculated ternary phase diagrams neglect solid solubility.

III.   EXPERIMENTAL RESULTS

All of the metals in this study, with the exception of Al and Co, demonstrated epitaxy on WSe_2. For most cases, thermal processing had little effect on the metal/WSe_2 structural relationship beyond decreasing the angular misalignment of already epitaxial systems. However, in the case of Pd/WSe_2, the metal overlayer changed from randomly oriented (polycrystalline) on deposition to being epitaxial with a large angular misalignment after annealing.

Aluminum

The Al/WSe$_2$ system, Figure 2, demonstrated a textured polycrystalline arrangement when deposited on WSe$_2$. The patterns show a large amount of double diffraction in the form of polycrystalline rings surrounding the diffracted WSe$_2$ spots, in addition to the center transmitted beam (covered by the beam block). This phenomenon is quite common in thicker and/or multi-layer films where electrons can be diffracted multiple times before exiting the sample. These results are quite different from our work on MoS$_2$, in which identically prepared samples showed Al to be epitaxial with an angular misalignment on deposition and perfectly epitaxial after annealing[24].
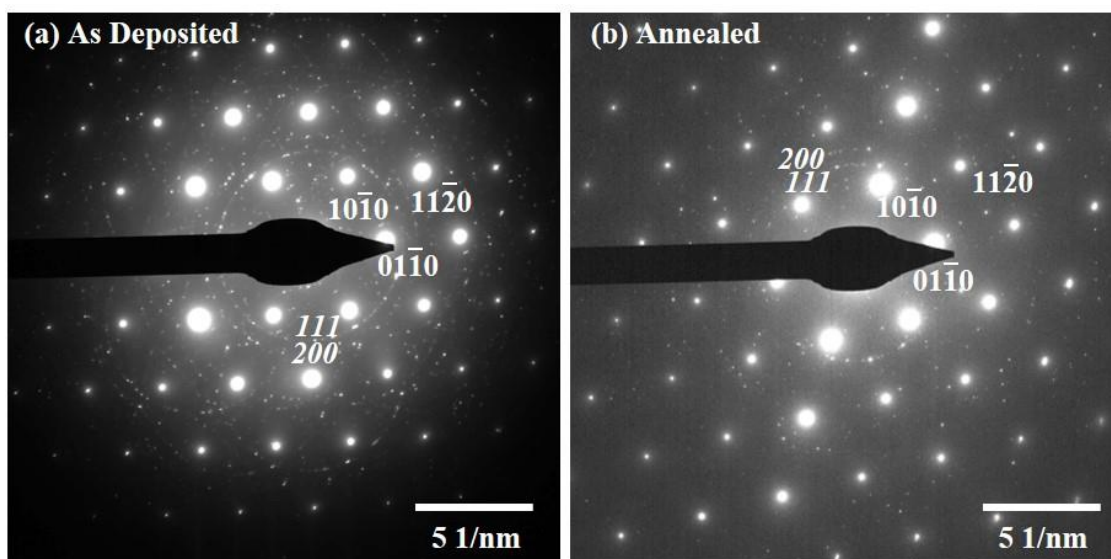

Figure 2. SAEDP of Al/WSe$_2$ in the (a) as-deposited condition and (b) annealed at 673 K for 4 h. WSe$_2$ plane assignments are located below the diffraction spots, and Al plane assignments are italicized and located next to the rings.

Nickel

Nickel was epitaxial on WSe$_2$ after deposition with an orientation relationship of Ni(111) ‖ WSe$_2$ (0001); Ni[2$\bar{2}$0] ‖ WSe$_2$ [11$\bar{2}$0]. As seen in Figure 3, the as-deposited sample demonstrated an angular misalignment of about ± 3º, which was reduced to ± 2º after annealing for 4 h. This angular misalignment accounts for the lines forming hexagons around the main WSe$_2$ spots. If the Ni were perfectly epitaxial, without angular misalignment, these lines would appear as spots. It is likely that the angular misalignment is reduced upon annealing due to grain coarsening, evidence of which can be seen in high angle annular dark field (HAADF) STEM imaging of the flakes in Figure 4.

The Ni/WSe$_2$ epitaxial relationship is an interesting discovery, since our previous work demonstrated that Ni was not epitaxial on MoS$_2$[24]. It seems that some differences in surface properties must exist between these two TMDs allowing for different epitaxial behavior of the deposited metal.
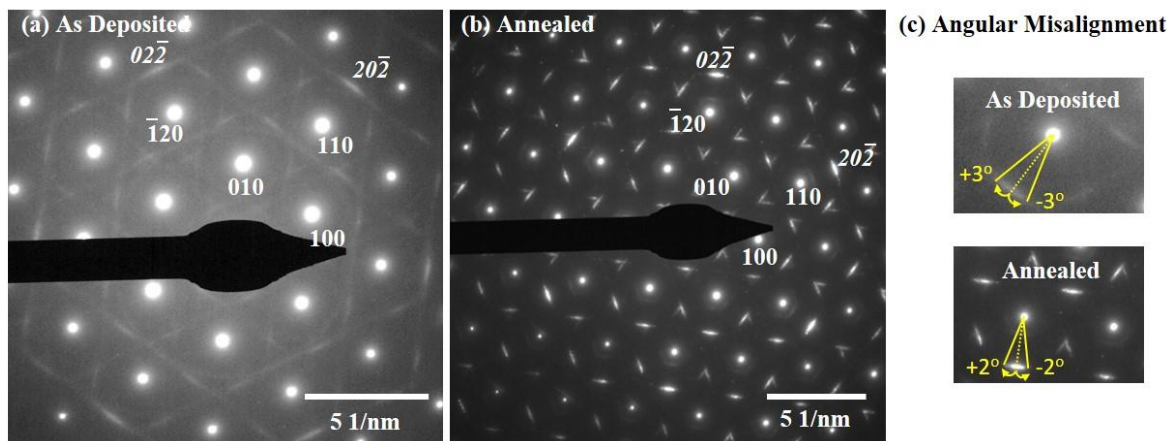
Figure 3. SAEDP of Ni/WSe$_2$ in the (a) as-deposited condition and (b) annealed at 673 K for 4 h. WSe$_2$ plane assignments are located below the diffraction spots, and Ni plane assignments are italicized and located above the diffraction spots. The angular misalignment measurement (c) is also included to highlight the difference between the as-deposited and annealed samples.
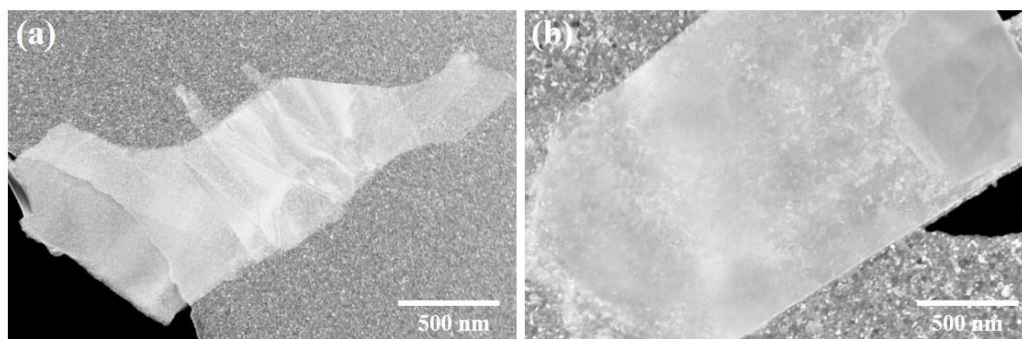

Figure 4. HAADF STEM of Ni/WSe$_2$ in the (a) as-deposited condition and (b) annealed at 673 K for 4 h. Metal grains are larger in the annealed condition, on the flake and on the substrate.

Palladium

Pd is another metal which showed a different epitaxial relationship with WSe$_2$ than with MoS$_2$. Literature and our previous work demonstrate that Pd is epitaxial on MoS$_2$ on deposition, with no major change to this structural relationship after annealing[11,12,24]. However, when

deposited on WSe$_2$, SAED patterns in Figure 5 showed Pd to be randomly oriented at room temperature. After annealing, Pd was observed to be epitaxial with a relationship of Pd(111) ‖ WSe$_2$ (0001); Pd[2$\bar{2}$0] ‖ WSe$_2$ [11$\bar{2}$0] and an angular misalignment over $\pm\,3^o$. It appears that the thermal energy of annealing was sufficient to allow atoms to rearrange epitaxially. Scanning electron microscopy of the surface in Figure 6 shows evidence of metal overlayer diffusion, in the form of agglomeration of Pd. From a practical standpoint, agglomeration is detrimental to electronic devices as it can break electrical connections. However, increase of grain size from annealing can be reduced in a couple different ways, such as making the metal layer thicker[38] and/or capping the contact with another layer[39].
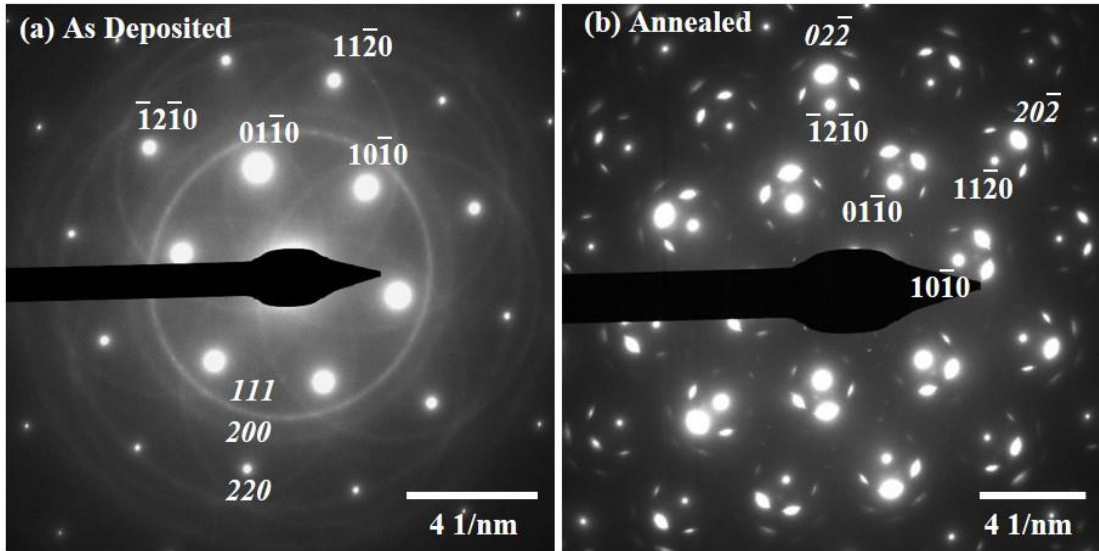

Figure 5. SAEDP of Pd/WSe$_2$ in the (a) as deposited condition and (b) annealed at 673 K for 5 h. WSe$_2$ plane assignments are located below the diffraction spots, and Pd plane assignments are italicized and located next to the rings or above the diffraction spots.
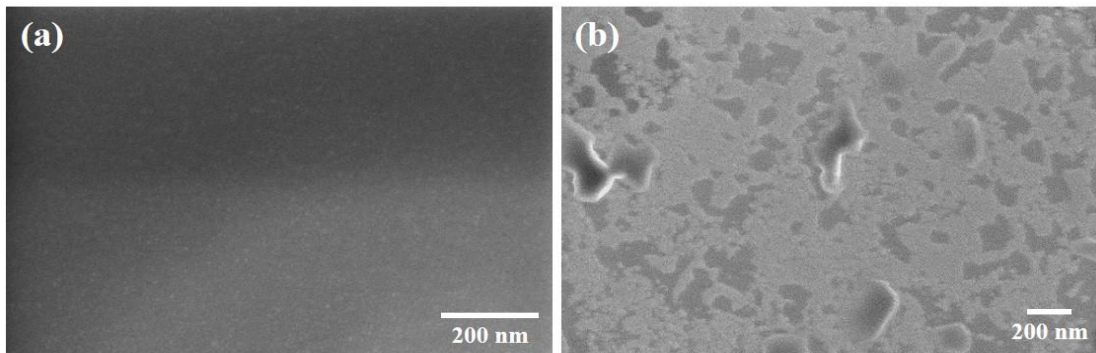
Figure 6. Surface SEM of Pd/WSe$_2$ in the (a) as deposited condition and (b) annealed at 673 K for 5 h. The as-deposited condition is nearly featureless, while the annealed condition demonstrates agglomeration of Pd.

Cobalt

Co was the only HCP metal examined in this work. Despite offering a similar close-packed plane with 6-fold symmetry as the other epitaxial metals, Co was polycrystalline on deposition and after annealing. The top surface of the sample was capped with a 20 nm layer of SiO$_2$ before annealing to help prevent oxidation; however, this cap could not prevent oxidation of Co above gaps in the holey carbon support. Some oxidation, as evidenced by additional rings in the SAED pattern, still occurred. Nevertheless, the polycrystalline Co rings were still visible in the SAED pattern in Figure 7. It should also be noted that not every spot in the very busy diffraction pattern in Figure 7 (b) was indexed; thus, it is possible that Co reacted with WSe$_2$ on annealing. However, our thermodynamic estimation of the Co-W-Se phase equilibria, discussed later, does not predict reaction. Although epitaxy of Co on MoS$_2$ has not been studied in the literature, our previous work demonstrates that one other HCP metal, Ru, demonstrated similar polycrystalline behavior, while Zn was epitaxial on MoS$_2$ [24].
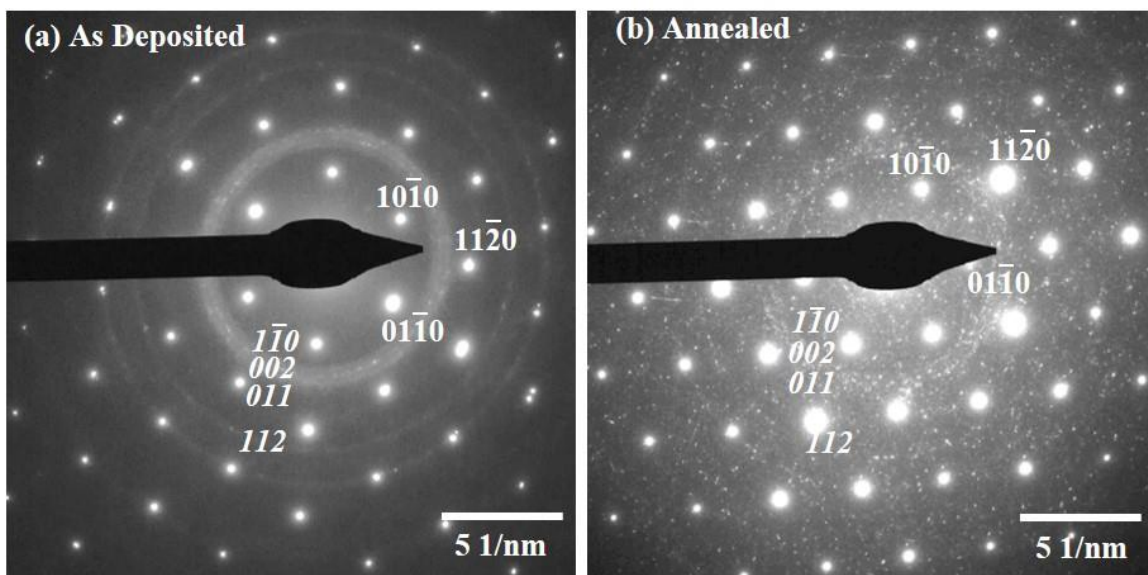
Figure 7. SAEDP of Co/WSe$_2$ in the (a) as deposited condition and (b) annealed at 673 K for 4 h. WSe$_2$ plane assignments are located below the diffraction spots, and Co plane assignments are italicized and located next to the rings.

Gold, Silver, and Copper

While not experimentally examined in this study, Au, Ag, and Cu have each shown an epitaxial relationship with WSe$_2$ in literature[5-8]. Thus, these metals are included in the discussion and theoretical calculations of the surface energies of metals on the WSe$_2$ surface. It is also important to note that all three of these metals are also epitaxial on MoS$_2$ [11,13-17,24].

IV. DISCUSSION

When compared to literature and our previous work[24,25], this investigation demonstrates that there are key similarities in the epitaxial behaviors of metals deposited on MoS$_2$ and WSe$_2$. Table 1 provides an overview of metal properties for the materials used in this study. As with MoS$_2$ systems[24], lattice mismatch has little effect on the epitaxy of metals deposited on WSe$_2$, with

mismatches near 30% still exhibiting epitaxial behavior. This finding is in stark contrast to typical epitaxial growth between two 3D materials, in which a large lattice mismatch results in defect formation to relieve stress. Instead, this quasi-van der Waals epitaxy, at the interface of a 2D and 3D material, appears to be insensitive to lattice mismatch, likely due to the lack of dangling bonds on the basal plane of the layered material. For this reason, misfit dislocations are not expected to form at the 2D/3D in interface, as with van der Waals epitaxy between 2D materials[40].

Table 1. Structural properties of metals examined for metal/WSe_2 epitaxy

Metal	Crystal Structure	WSe_2 Lattice Mismatch
Au	**FCC**	**13.8%**
Ag	**FCC**	**13.6%**
Cu	**FCC**	**28.4%**
Al	FCC	14.6%
Ni	**FCC**	**31.7%**
Pd	**FCC**	**19.3%**
Co	HCP	30.9%

*** Epitaxial metals are written in bold font***

Surface Mobility of Metals on WSe_2

Besides a match in crystallographic symmetry, in order for sputtered metal atoms to arrange epitaxially on a TMD surface, they must be able to diffuse to reach low energy positions. Just as for MoS_2[24], the effect of metal surface diffusion on epitaxy can be gauged using the barrier to surface diffusion on WSe_2, as provided in Table 2 for the metals in this study. The barrier to

surface diffusion describes the minimum energy barrier that metal atoms must overcome in order to diffuse on the TMD surface. Values are calculated using DFT simulations by computing the barrier for diffusion between the high symmetry sites shown in Figure 1, and are found to vary on different TMDs[25].

As shown in Table 2, the metals that were epitaxial on WSe_2, either from literature or from the experimental work of this study, each demonstrated a low barrier to surface diffusion (≤ 0.51 eV). Gold, epitaxial on WSe_2 in the literature[6-8], presented the lowest barrier to surface diffusion at 0.04 eV. The work in the literature reveals the importance of deposition rate and substrate temperature on Au/WSe_2 epitaxy[6-8]. In our case, the deposition rate was kept at 1 Å/s for all systems, and the substrate temperature, measured by a thermocouple, was kept under 40 °C for all deposited metals. Though important, deposition rate and substrate temperature are not deciding factors in whether or not we observed epitaxy under conditions typical for the fabrication of metal/semiconductor contacts.

One of the non-epitaxial metals that was studied, Co, exhibited a barrier to surface diffusion that was quite high at 0.90 eV. This value was nearly double that of Ni, which had the highest barrier to surface diffusion for metals epitaxial at room temperature in this study. Thus, despite having the requisite basal plane geometry as an HCP metal, Co atoms were not sufficiently mobile to rearrange epitaxially on the WSe_2 surface. The other non-epitaxial metal, Al, exhibited a much lower barrier to surface diffusion (0.22 eV); however, our work reveals that the lack of epitaxy in this system can be addressed by another controlling variable discussed in the following section.

Table 2. Surface mobility of metal atoms on WSe_2.

Metal	Barrier to Surface Diffusion (eV)
Au	**0.04**
Ag	**0.12**
Cu	**0.13**
Al	0.22
Ni	**0.47**
Pd	**0.51**
Co	0.90

*** *Epitaxial metals are written in bold font* ***

Predictions of Metal-WSe₂ Phase Equilibria

Our analysis to this point assumes that the metals are unreactive on WSe_2. However, we could not find any published condensed phase diagrams for the metal-W-Se systems, which would be helpful for identifying systems in which there is a driving force for reaction between the metal and WSe_2. Therefore, this study utilized published thermodynamic data to calculate ternary phase diagrams for several metal-W-Se systems at 25 °C to classify systems as: WSe_2 dominant, metal selenide dominant, or indeterminant. The classification of the metals in this study, in terms of both thermodynamic and epitaxial relationships, are provided in Table 3, and Figure 8 provides examples of calculated phase diagrams for each classification.

Table 3. Classification of predicted ternary phase diagrams for metal/WSe₂ systems

WSe$_2$ Dominant	Metal Selenide Dominant	Indeterminant
Au	Al	**Ni**
Ag		**Pd**
Cu		
Co		

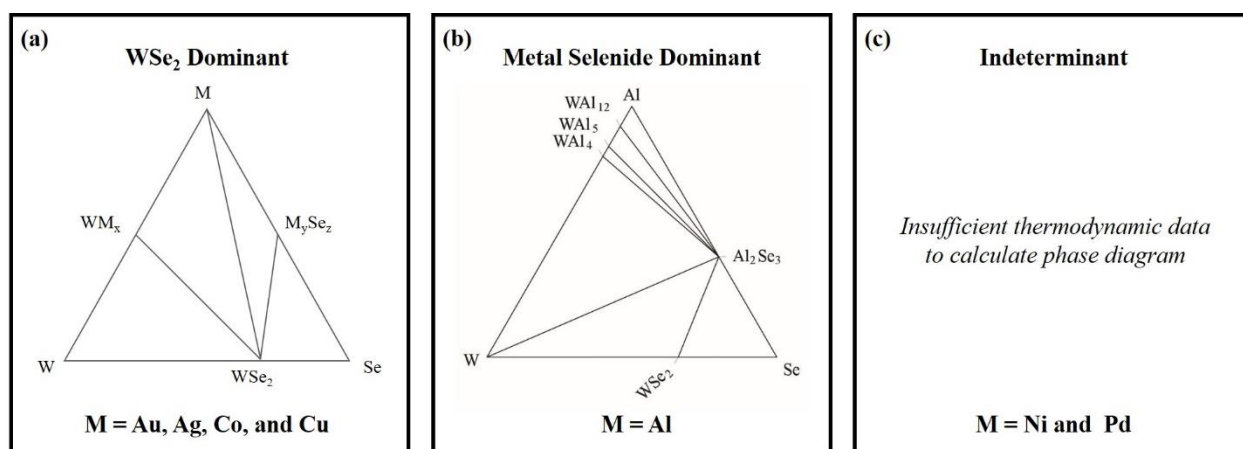*** *Epitaxial metals are written in bold font* ***

Figure 8. Example ternary phase diagrams for metal/WSe$_2$ systems. (a) For WSe$_2$ dominant systems, WSe$_2$ is in equilibrium with the elemental metal. Both WM$_x$ and M$_y$Se$_z$ phases could also be present. (b) In the only metal selenide dominant system (Al), the calculated ternary phase diagram shows that all phases are in equilibrium with Al$_2$Se$_3$. (c) A few systems were indeterminant, as they required additional thermodynamic data for classification.

For WSe$_2$ dominant systems, WSe$_2$ is in equilibrium with the elemental metal as well as the binary intermetallic compounds that exist. Figure 8 (a) provides an example of a generic ternary phase diagram for this classification. All epitaxial metals reported in literature (Au, Ag, Cu) fall into this category. Although Co is also predicted to be unreactive with WSe$_2$, its lack of epitaxy can be attributed to the low mobility of Co atoms on the WSe$_2$ surface.

Al/WSe$_2$ was the only metal selenide dominant system in this study. This type of system is characterized by phase equilibrium between a very stable metal selenide and pure W metal. The calculated phase diagram for the Al-W-Se system is provided in Figure 8 (b). In the case of Al/WSe$_2$, there is a driving force for Al to react with WSe$_2$ to form Al$_2$Se$_3$ and W metal or aluminides.

Interestingly, Al did not demonstrate an epitaxial relationship with WSe$_2$, either before or after annealing, even though it has the FCC structure and the barrier to diffusion of Al on the surface of WSe$_2$ is low. This discrepancy can be attributed to an interfacial reaction between Al and WSe$_2$. Figure 9 shows cross-sectional TEM and EDS of an as-deposited and annealed flake beneath Al metal. The elemental mapping of both as-deposited and annealed samples in Figure 9 (c)-(l) demonstrates that both W and Se have intermixed with the Al layer so that there is an Al$_x$Se$_y$ layer and regions with an Al$_x$W$_y$ phase as well as elemental W (embedded) and Al (on top). In the cross-sectional TEM in Figure 9 (a-b), it is apparent that the Al$_x$Se$_y$ compound is amorphous in both the as-deposited and annealed samples, which is why this reaction product was not observed in plan-view electron diffraction patterns. Also, the amount of elemental W and Al$_x$W$_y$ phase is believed to be small enough that it was not readily detected by plan-view TEM.

The final classification, indeterminate, includes metals for which too little thermodynamic data exists to predict phase equilibria. Two metals in this study (Ni and Pd) fall into this category. Both Ni and Pd were epitaxial, and neither showed any evidence of reacting with WSe$_2$ using plan-view TEM, either on deposition or after annealing, but if such a reaction occurred, it did so without disrupting the orientation of the remaining Ni and Pd or fully consuming the metals.
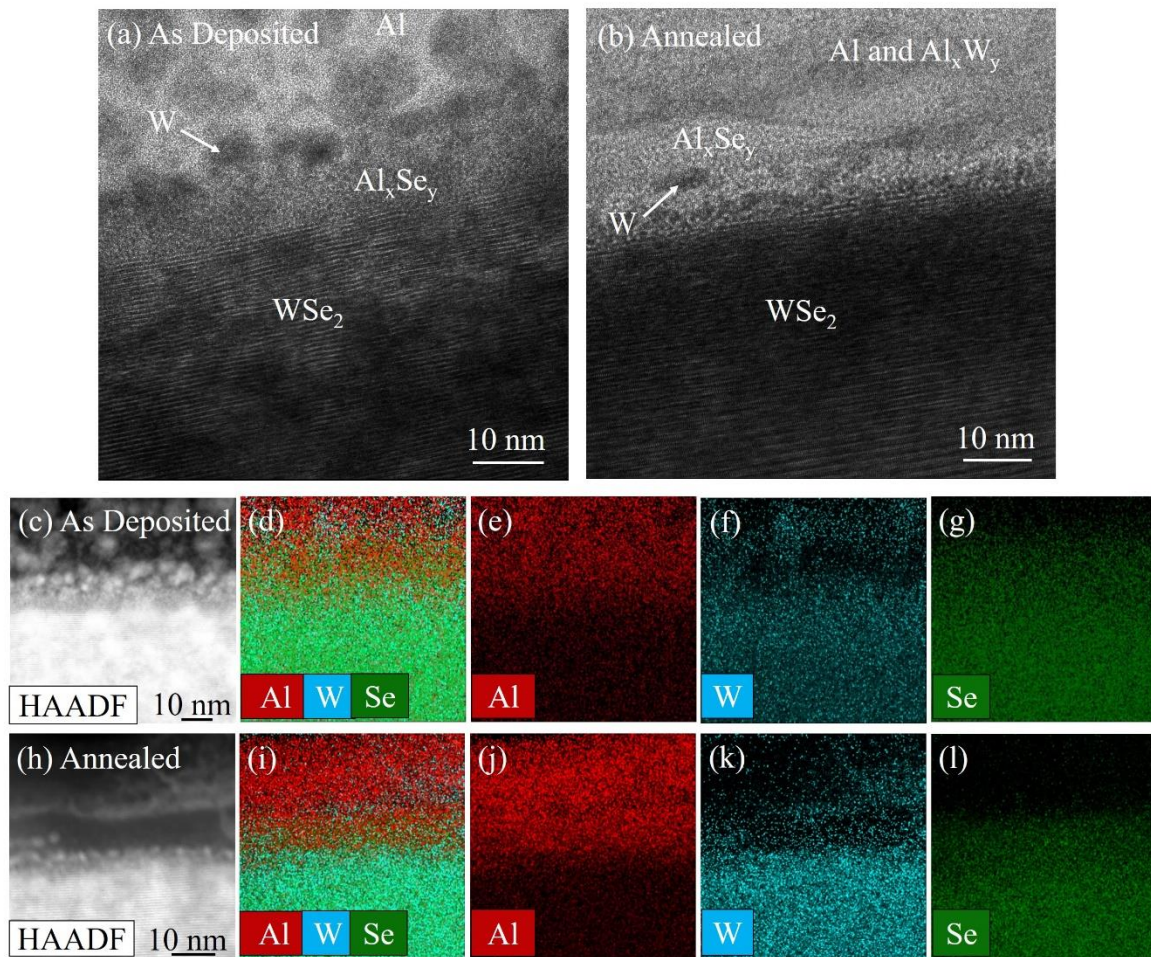
Figure 9. Cross-sectional BF TEM of Al/WSe$_2$ (a) as-deposited and (b) annealed at 673 K for 4 h. HAADF STEM and EDS mapping of the as-deposited (c)-(g) and annealed conditions (h)-(l) shows W and Se migration.

Comparison of Metal/MoS$_2$ and Metal/WSe$_2$ systems

This study also revealed key differences between a few metal/WSe$_2$ and metal/MoS$_2$ epitaxial relationships. Three metals (Al, Ni and Pd) demonstrated significantly different behaviors when deposited on these two different TMDs. In the case of Al, the metal demonstrated epitaxy when deposited on MoS$_2$ but polycrystalline behavior when deposited on WSe$_2$. For Ni, where

Ni/MoS$_2$ was polycrystalline and showed some signs of diffusion into the MoS$_2$ layers[24], Ni/WSe$_2$ was epitaxial on deposition with no signs of reaction or diffusion. Lastly, Pd/MoS$_2$ was epitaxial before and after annealing[11,12,24]. However, Pd/WSe$_2$ was epitaxial only after annealing.

The different behavior of Al on MoS$_2$ and WSe$_2$ can be attributed to differences in reactivity. While thermodynamics favor a room-temperature reaction and experimental results of an annealed sample show evidence of a reaction in Al/WSe$_2$ contacts, our previous work did not show any evidence of a reaction in Al/MoS$_2$[24]. For the Ni and Pd systems, the metals demonstrated different behavior on WSe$_2$ than on MoS$_2$, consistent with a clear difference in the energy barrier to metal surface diffusion on MoS$_2$ compared to WSe$_2$, as seen in Table 4. When the energy barrier is higher (0.51 eV for Pd on WSe$_2$ and 0.85 eV for Ni on MoS$_2$), the metal is polycrystalline on deposition; when the energy barrier is lower (0.47 eV for Pd on MoS$_2$ and 0.43 eV for Ni on WSe$_2$), the metal is epitaxial on deposition. To date, Pd/WSe$_2$ is the only system observed to transform from polycrystalline to epitaxial after annealing. Considering that the barrier to surface diffusion in the polycrystalline system was only slightly higher than in its epitaxial system, we can conclude that the thermal energy of annealing was sufficient to overcome this barrier and allow the polycrystalline Pd atoms to rearrange epitaxially. Thus, even the differences between metal structural relationships between MoS$_2$ and WSe$_2$ further confirm our conclusions that metal surface diffusion, in addition to hexagonal basal geometry, are critical in controlling metal/TMD epitaxy. Furthermore, these results show that calculating the barrier to surface diffusion can be used to predict which FCC and HCP metals will be epitaxial on TMDs for unreactive interfaces.

Table 4. Barriers to surface diffusion of Ni and Pd on MoS$_2$ and WSe$_2$

19

Metal	Crystal Structure	Barrier to Surface Diffusion (eV) on MoS$_2$[25]	Barrier to Surface Diffusion (eV) on WSe$_2$
Ni	FCC	0.85	**0.47**
Pd	FCC	**0.43**	0.51

*** Room-temperature epitaxial metals are written on bold font. Note that Pd was epitaxial on WSe$_2$ after annealing at 673 K for 4 h (Ni) and 5 h (Pd)***

V. SUMMARY

This study revealed that Ni was epitaxial on WSe$_2$ on deposition at room temperature, while Al, Co, and Pd were polycrystalline on WSe$_2$ on deposition. Pd/WSe$_2$ was the only system to become epitaxial during annealing. All epitaxial metals were FCC and demonstrated the following orientation relationship: M(111) || WSe$_2$(0001); M[2$\bar{2}$0] || WSe$_2$ [11$\bar{2}$0]. Correlating our experimental work and known epitaxial metals from the literature with theory revealed that multiple interdependent factors control epitaxial growth of metals deposited on TMDS. First, the metal must have suitable symmetry for epitaxy. Secondly, it must be energetically favorable for metal atoms to diffuse on the TMD surface, a metric aptly described by the energy barrier to surface diffusion. Finally, the metals cannot react with the underlying TMD material. The results of this study of metals on WSe$_2$ are consistent with our earlier study of metals on MoS$_2$. Thus, we expect that our approach for evaluating the factors controlling metal epitaxy on TMDs can be applied to predict epitaxy on other 2D materials.

VI. ACKNOWLEDGEMENTS

VII.   REFERENCES

1. Yazyev, O.; Kis, A. *Mater. Today* **18** (2015): 20.

2. Cheng, R.; Jiang, S.; Chen, Y.; Liu, Y.; Weiss, N.; Cheng, H.-C.; Wu, H.; Huang, Y.; Duan, X. *Nat. Commun.* **5** (2014): 5143.

3. Akinwande, A.; Petrone, N.; Hone, J. *Nat. Commun.* **5** (2014): 5678.

4. Yao, Z.; Liu, J.; Xu, K.; Chow, E. K. C.; and Zhu, W. *Sci. Rep.* **8** (2018): 5221.

5. Jaegermann, W.; Pettenkofer, C.; Parkinson, B. A. *Phys. Rev. B* **42** (1990): 7487

6. Klein, A.; Pettenkofer, C.; Jaegermann, W.; Lux-Steiner, M.; Bucher, E. *Surf. Sci.* **321** (1994): 19.

7. Rettenberger, A.; Bruker, P.; Metzler, M.; Mugele, F.; Matthes, Th.W.; Böhmisch, M.; Boneberg, J.; Friemelt, K.; Leiderer, P. *Surf. Sci.* **402–404** (1998): 409.

8. Nicolay, G.; Claessen, R.; Reinert, F.; Strocov, V. N.; Hüfner, S.; Gao, H.; Hartmann, U.; Bucher, E. *Surf. Sci.* **432** (1999): 95.

9. Jaegermann, W.; Ohuchi, F. S.; Parkinson, B. A. *Surf. Sci.* **201** (1988): 211.

10. Jaegermann, W.; Ohuchi, F. S.; Parkinson, B. A. *Surf. Interface Anal.* **12** (1988): 293.

11. Gillet, M.; Renou, A. *Thin Solid Films* **52** (1978): 23.

12. Perrot, E.; Humbert, A.; Piednoir, A.; Chapon, C.; Henry, C. R. *Surf. Sci.* **445** (2000): 407.

13. Jesser, W. A.; Kuhlmann-Wilsdorf, D. *Acta Metall. Mater.* **16** (1968): 1325.

14. Stowell, M. *J. Thin Solid Films* **12** (1972): 341.

15. Kamiya, Y.; Uyeda, R. *Acta Crystallogr.* **14** (1961): 70.

16. Poppa, H. Z. *Naturforsch.* **19** (1954): 835.

17. Yagi, K.; Takayanagi, K.; Kobayashi, K.; Honjo, G. *J. Cryst. Growth* **28** (1975): 117.

18. Bortz, M. L.; Ohuchi, F. S.; Parkinson, B. A.; *Surf. Sci.* **223** (1989): 285.

19. Das, S.; Chen, H. Y.; Penumatcha, A. V.; Appenzeller, *J. Nano Lett.* **13** (2013): 100.

20. Smyth, C. M.; Addou, R.; McDonnell, S.; Hinkle, C. L.; and Wallace, R. M. *2D Mater.* **4** (2017): 025084.

21. Tung, R. T. *Phys. Rev. Lett.* **84** (2000): 6078.

22. Tung, R. T. *J. Vac. Sci. Technol. B* **11** (1993): 1546.

23. Tung, R. T. *Phys. Rev. Lett.***52** (1984): 461.

24. Domask, A.; Cooley, K.; Kabius, B.; Abraham, M.; Mohney, S. *Crys. Growth Des.* **18** (2018): 3494.

25. Saidi, W. *Crys. Growth Des.* **15** (2015): 3190.

26. Perdew, J. P.; Burke, K.; Ernzerhof, M. *Phys. Rev. Lett.* **77** (1996): 4.

27. Blochl, P. E. *Phys. Rev. B.* **50** (1994): 17953.

28. Kresse, G.; Joubert, D. *Phys. Rev. B* **59** (1999): 1758.

29. Henkelman, G.; Uberuaga, B. P.; Jónsson, H. *J. Chem. Phys.* **113** (2000): 9901.

30. Saidi, W. A. *Crys. Growth Des* **15** (2015): 642.

31. Saidi, W. A., *J. Chem. Phys.* **141** (2014): 094707.

32. Schmid-Fetzer, R. *JEM* **17** (1988): 193.

33. www1.asminternational.org,. ASM Alloy Phase Diagrams Database http://www1.asminternational.org/asmenterprise/apd/ (accessed Sep 10, 2015).

34. Boer, F. *Cohesion In Metals*; North-Holland: Amsterdam, 1988.

35. Kubaschewski, O.; Alcock, C.; Spencer, P.; Kubaschewski, O. *Materials Thermochemistry*; Pergamon Press: Oxford, 1993.

36. Olin, A. *Chemical Thermodynamics Of Selenium*; Elsevier: Amsterdam, 2005.a

37. O'Hare, P.; Lewis, B.; Parkinson, B. *J. Chem. Thermodyn.* **20** (1988): 681.

38. Boragno, C.; Buatier de Mongeot, F.; Felici, R.; and Robinson, I. K. *Phys. Rev. B* **79** (2009): 155443.

39. Abraham, M. and Mohney, S. E. *J. Appl. Phys.* **122** (2017): 115306.

40. Jaegermann, W.; Klein, A.; Pettenkofer, C. In *Electron Spectroscopies Applied to Low-Dimensional Materials*; Hughes, H. P., Starnberg, H. I., Eds.; 2000; pp 317.